

Flow Testing of a MEMS Floating Element Shear Stress Sensor

Zhengxin Zhao¹

Mechanical Engineering, Tufts University, Medford, MA 02155

Kurtis R. Long²

Aerospace Computing Incorporated, Mountain View, CA 94035

Judith Gallman³

Spirit Aerosystems, Wichita, KS 67210

and

Robert D. White⁴

Mechanical Engineering, Tufts University, Medford, MA 02155

A MEMS floating element shear stress sensor array has been tested under a turbulent boundary layer in an 38 x 38 cm test-section inflow wind tunnel. The MEMS sensor itself is a 1 cm² chip with 256 nickel floating elements arrayed in parallel. Real time shear was measured as tunnel free stream velocity varied from no flow up to 62 m/s. Shear stresses up to 6.5 Pa were measured, consistent with expectations based on the measured boundary layer profile and zero pressure gradient flat plate boundary layer theory. Sensor sensitivity was 90 aF/Pa, very similar to theoretical predictions. Resolution was 1 Pa/Hz^{1/2}. Data rate was 3 samples/second. Orientation dependence of the sensor output was verified, demonstrating the ability to measure direction as well as magnitude of the shear stress.

I. Introduction

A variety of methods exist for skin friction measurement [1-3]. Techniques such as oil film interferometry give good coverage of surfaces, but can be difficult to implement and do not provide real time or unsteady data [4]. Hot film methods can provide real time information but may be difficult to calibrate in an absolute sense. In addition, hot film methods do not provide a directional measurement [5-7].

An alternative technology for shear measurement is the MEMS-based floating element method [8-12]. In this measurement technology, a micromachined plate or shuttle is suspended using micromachined beam tethers. Under the influence of hydrodynamic forces, this “floating element” experiences a lateral deflection. The motion may be detected using capacitance change, piezoresistance, or optical methods. MEMS floating elements have the advantages of ease of use, high spatial and temporal resolution, and are a “direct” measurement technology insofar as they respond to momentum transfer at the wall. However, MEMS floating element sensors suffer from some drawbacks, including sensitivity to pressure gradients, potential for misalignment, and a possible lack of robustness to water or particle impingement [1,13].

Our group previously reported a nickel MEMS floating element sensor array on a chip for surface shear measurement [14,16]. A fabrication process, simple model, and experimental sensitivity to flow was demonstrated in a laminar flow cell. In this paper we describe the first demonstration of operation of a MEMS floating element sensor in a wind tunnel flow environment.

¹ Research Assistant, Tufts University, Mechanical Engineering, Medford, MA 02155, AIAA Member

² Senior Research Engineer, Aerospace Computing Incorporated, Mountain View, CA 94035

³ Associate Technical Fellow, Spirit Aerosystems, Wichita, KS 67210, Senior AIAA Member

⁴ Associate Professor, Tufts University, Mechanical Engineering, Medford, MA 02155, Senior AIAA Member

II. Design

As described in [14, 16], the floating element sensor has a movable center shuttle suspended by folded beam that act as a spring and support the shuttle. The sensor responds to hydrodynamic forces by deflecting laterally. The lateral deflection is measured by a differential capacitance change between the comb fingers fabricated on either side of the sensor.

The mechanical structure of the folded beams can be seen in Figure 1. The four inner beams and the outer fingers are fixed on the substrate through the anchors. The folded beam structure is employed to reduce the effects of residual stresses introduced during manufacturing, as these stresses may relax out after structure release. The dimensions of the element are given in Table 1.

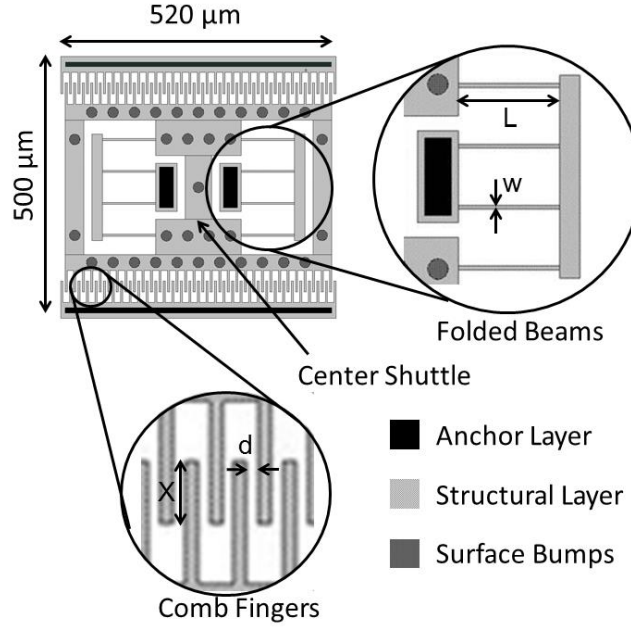


Figure 1: Diagram of the mechanical structure of the floating element sensor.

Table 1. As-manufactured dimensions of the floating element sensor.

Finger gap, d (μm)	2.88
Finger width (μm)	5.13
Number of comb fingers per element, N	64
Thickness of structure, t (μm)	8.8
Width of folded beam, w (μm)	5.13
Length of folded beam, L (μm)	99.2
Height of bump (μm)	11.7
Diameter of bump (μm)	24.7
Air gap separation (μm)	5.2
Shuttle top area, A_m (mm^2)	0.096

Flow forces acting on the center shuttle will bend the folded beams and create shuttle displacement primarily in the direction of the flow. Considering the shuttle and the fingers as a rigid body, the sensor stiffness in the lateral in-plane direction is easily related to the geometry of the beams

$$K_x = 2Et \left(\frac{w}{L} \right)^3 \quad (1)$$

where E is the Young's modulus of the structural material (Nickel), and w , t , and L are the width, thickness and length of each beam, as shown in Figure 1. The aspect ratio (t to w) is designed to be high to minimize out-of-plane motion.

Interdigitated overlap of the comb fingers determines the total active capacitance of the element,

$$C = 2N \frac{\epsilon t}{d} X \quad (2)$$

where N is the number of fingers on the element, ϵ is permittivity of air, t is the thickness of the structure, d is the finger gap and X is the overlap length. This ignores capacitive fringing effects at the edges and assumes no out-of-plane motion. Thus, the differential change of capacitance for the element depends on the displacement δX only,

$$\delta C = 2N \frac{\epsilon t}{d} \delta X \quad (3)$$

where δX is the displacement of the shuttle. The sensitivity, in terms of capacitance change, of the floating element to a constant applied force is thus

$$S_1 = \frac{\partial C}{\partial F} = \frac{\partial C}{\partial X} \frac{\partial X}{\partial F} = \frac{\partial C}{\partial X} \frac{1}{K_x} = \frac{N \epsilon L^3}{E d w^3} \quad (4)$$

The structure will respond to forces applied to the shuttle arising from interaction with the flow field. For a sensor that includes gaps, sensor surface topology, intentional and unintentional surface roughness, and packaging topology, it is expected that the steady fluidic force may depend on both the time average local wall shear stress, the local streamwise pressure gradient in the flow, and the details of the geometry at the microscale [17]. It is also possible that the compressibility of the flow (Mach number) may play a role, and, in the case of boundary layer flows, the boundary layer thickness may be important.

As a simplified model, consider the sensor to have an effective rectangular shape, and to be acted on by the local surface shear stress and the pressure gradient present in the flow, as diagrammed in Figure 2.

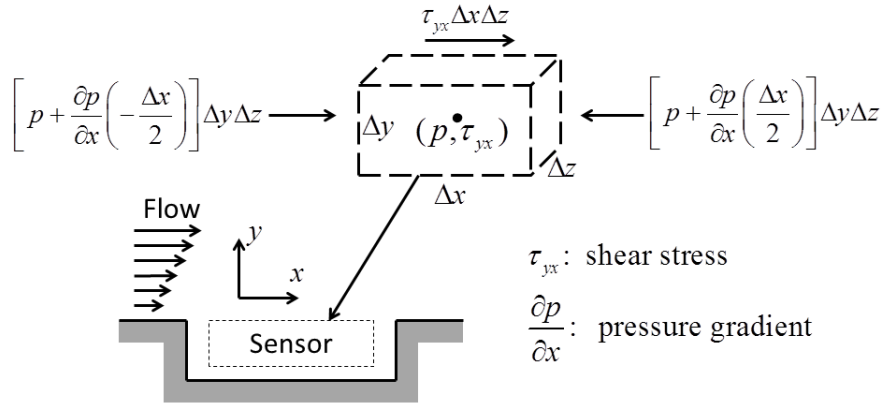


Figure 2: Simple model of the flow interaction with the shear sensor including pressure gradient and surface shear.

It is emphasized that the effective size of the element, Δx by Δy by Δz , is not identical to the physical size of the element. These effective dimensions will be determined experimentally, and to first order account for the unknown details of the microscale flow around the element. They can also account for small manufacturing nonuniformities or imperfect packaging, such as a slightly misaligned sensor. It is likely that these dimensions will be of the same order of magnitude as the physical size of the element, but certainly are not expected to be identical to its physical size. Experimental work not reported here suggests that for this device, the effective surface area, $\Delta x \Delta z$, will be

similar to the physical surface area A_m [16]. However, the effective volume, $\Delta x \Delta y \Delta z$, may be more than ten times the physical volume, $A_m t$ [16].

Given this model, the fluidic force acting on the element will be

$$F = \tau_{yx} \cdot \Delta x \Delta z - \left(\frac{\partial p}{\partial x} \right) \cdot \Delta x \cdot (\Delta y \Delta z) \quad (5)$$

By combining equations (4) and (5), the differential sensitivity of a single element to the two flow variables can then be written

$$S_2 = \frac{\partial C}{\partial \tau_{yx}} = \frac{\partial C}{\partial F} \frac{\partial F}{\partial \tau_{yx}} = \frac{N \varepsilon L^3}{E d w^3} \Delta x \Delta z \quad (6)$$

$$S_3 = \frac{\partial C}{\partial (\partial p / \partial x)} = \frac{\partial C}{\partial F} \frac{\partial F}{\partial (\partial p / \partial x)} = \frac{-N \varepsilon L^3}{E d w^3} \Delta x \Delta y \Delta z \quad (7)$$

where S_2 is the sensitivity to shear, and S_3 is the sensitivity to pressure gradient.

With this model in mind, in an effort to increase the sensitivity of the sensor by increasing the effective area of interaction with the flow (Δx , Δy , and Δz), surface bumps were fabricated on the top of the shuttle. As shown in Figure 1, 35 cylindrical bumps, each 12 μm high with a diameter of 25 μm , were fabricated in a distributed pattern. Modeling work suggests that these bumps do indeed increase sensitivity; although it is possible they may increase pressure gradient sensitivity (undesirable) more than surface shear sensitivity [17].

In anticipation of a future goal of measuring local spatial variation in unsteady shear, the 1 cm square chip was designed to include an array of 16 by 16 elements. The 256 elements were subdivided into 16 groups of 16 elements each, so that each group has a 4 by 4 pattern of elements as shown in Figure 3.

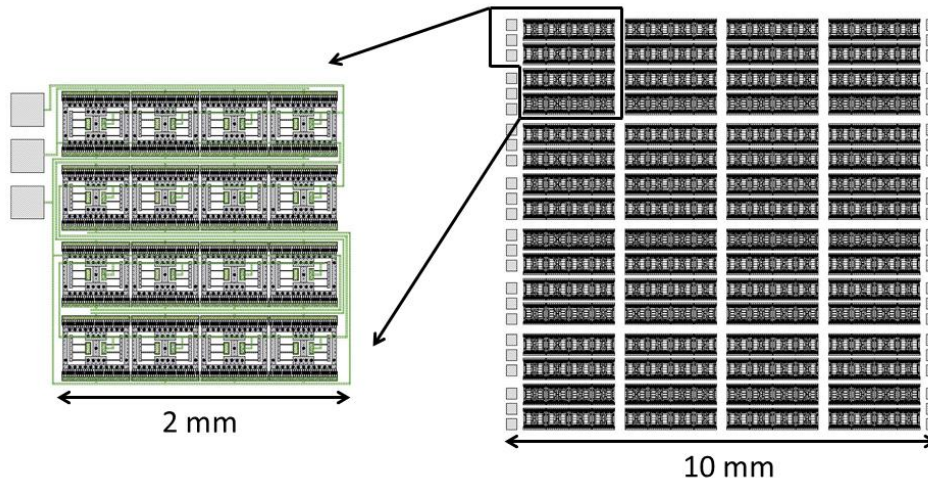


Figure 3: Layout of the 1 cm² array chip. 256 elements are arranged into 16 groups of 16 elements. Each group is independently addressable.

Each group has independent connections routed to three electrical pads for the top combs, bottom combs, and common (center shuttle) electrodes. The groups are approximately 2 mm x 2 mm in size, thus the spatial resolution for shear measurements of the array-on-a-chip is on the order of 2 mm. The local shear stress of a group or average shear of the whole chip can be measured separately. This allows the end user to trade off between spatial resolution and sensitivity. In addition, a major benefit of the array architecture is that failure of a single element or single group, either during fabrication or during operation, does not destroy the functionality of the entire chip. This may

be a highly desirable feature for sensors deployed in harsh operating environments where single elements may be lost to particulates or moisture, but the chip continues to function, albeit with reduced sensitivity.

A schematic of the system electronics is shown in Figure 4. An AD7745 [Analog Devices, Wilmington, MA] capacitance to digital converter chip is used to measure the differential capacitance between the top and bottom electrodes on the MEMS chip. The chip operates from a single 5V supply, and uses an AC excitation and a sigma delta modulator to measure differential capacitance changes. The AD7745 is expected to provide a resolution of $1.5 \text{ aF}/\sqrt{\text{Hz}}$, according to the manufacturer.

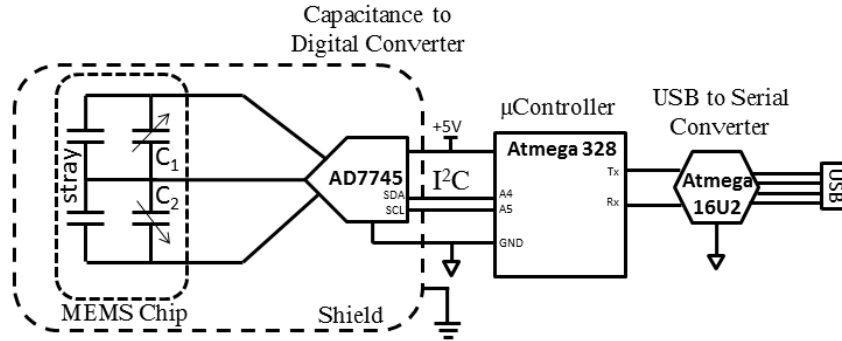
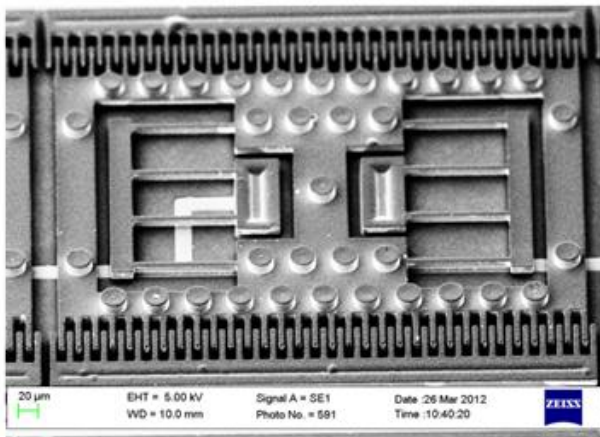
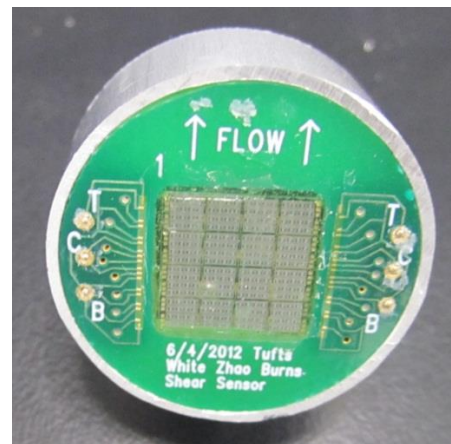


Figure 4: Readout electronics use an AD7745 capacitance to digital converter to perform differential capacitance measurements. Communication is via I²C to a microcontroller which then communicates over USB.

The AD7745 communicates with an Atmega328 microcontroller using the two wire I²C protocol. The microcontroller then communicates with a computer over USB via an Atmega16U2 configured as a serial to USB converter. The speed of the system is limited by the conversion time of the AD7745. The results shown here are for the slowest conversion time, 109.6 ms. Shorter conversion times down to 11 ms can be used, but result in a lower capacitance resolution.



(a)



(b)

Figure 5: (a) SEM image of a single element in the sensor array. (b) Photograph of the packaged chip. This is a 25 mm diameter, 13 mm long tube with the 1 cm² chip in the center. Signal processing electronics are inside the tube with a 4 pin connector on the back for power and 2 wire I²C digital communication.

The microfabrication of the device has been described previously [14, 16], and need not be repeated here. The chip is packaged in a printed circuit board using potting epoxy and connected on the frontside using either gold wirebonds or thin film conductive ink. This results in a maximum surface topology of approximately 0.1 mm along the edges of the chip. The circular PCB is mounted into a 25 mm diameter, 13 mm long aluminum tube. The AD7745 capacitance to digital conversion IC is packaged inside the aluminum tube on a second circular PCB. A

four pin connector on the back of the tube provides power and 2 wire I2C digital communication with the AD7745. A SEM image of an individual element and a photograph of the packaged sensor are shown in Figure 5.

III. Experimental Results

For flow testing, the sensor was flush mounted into the floor plate of a laboratory wind tunnel in the fluid mechanics lab at NASA Ames Research Center. The tunnel is an open circuit indraft tunnel with a 38 x 38 cm square cross-section with a maximum flow speed of 62 m/s. A settling chamber with honeycomb and 8 mesh screens, a rounded bell mouth inlet, and a smooth 0.7 m long square to round diffuser contribute to a low turbulent intensity at the inlet to the test section. Suction to produce flow is provided by a 75 hp centrifugal blower. The MEMS shear sensor was mounted at a location 65 cm downstream from the exit of the contraction section. The test setup is shown in Figure 6.

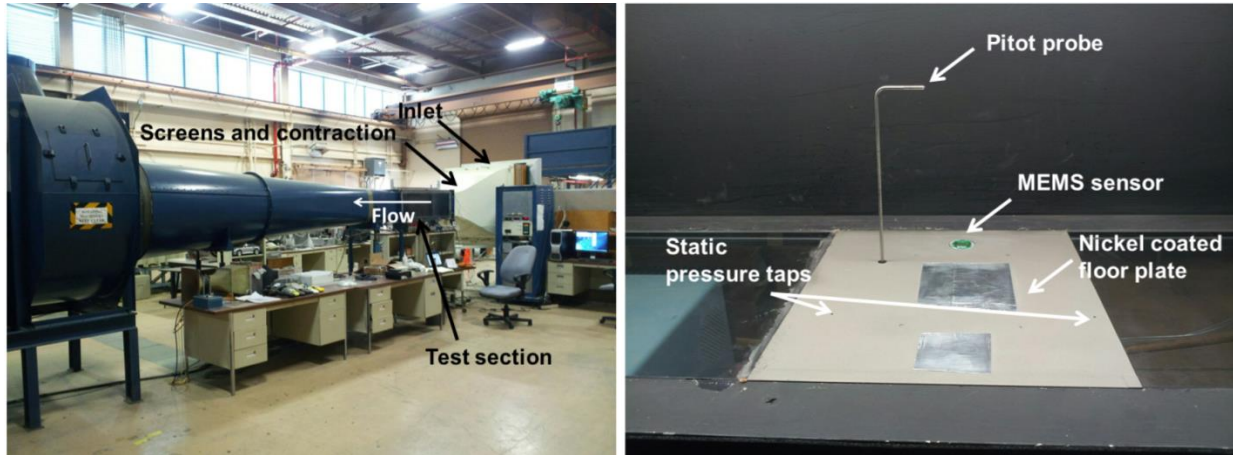


Figure 6: Photographs of the flow facility and the test section. The MEMS sensor is flush mounted in a nickel painted acrylic plate in the floor of the test section, 65 cm from the end of the contraction. A pitot probe is used to measure the free stream velocity and boundary layer profile.

The floor plate used in the experiment was cast acrylic. In initial testing, the sensor exhibited substantial drift and hysteresis. It was determined that this was due to tribological charging of the insulating acrylic plate. The effect had not been observed when testing in a conducting aluminum plate. The sensitive capacitance measurement used in this device has the potential to be very sensitive to charging in the local environment. To combat this problem, the acrylic plate was painted with a conductive nickel-based spray paint, and grounded. This surface treatment removed the drift and hysteresis.

The tunnel was run at four discrete flow speeds by controlling blower RPM. During testing, a pitot/static probe was used to measure dynamic pressure near the flow centerline to estimate free stream velocity. The dynamic pressure and shear stress were recorded simultaneously during the tests at 1 sample per second. Table 2 gives the four conditions. The flow speed is the measured speed from the pitot/static probe, assuming an air density of $\rho=1.2 \text{ kg/m}^3$. Mach number and Reynold's number based on plate length were computed from the flow speed using a speed of sound $c=343 \text{ m/s}$ and dynamic viscosity for air of $\nu=1.5 \cdot 10^{-5} \text{ m}^2/\text{s}$. The skin friction coefficient and boundary layer thickness were estimated from a $1/7^{\text{th}}$ power law [15]

$$C_f = 0.027 \text{Re}_x^{-1/7} \quad (8)$$

$$\delta = 0.16x \text{Re}_x^{-1/7} \quad (9)$$

Table 2. Flow conditions for tunnel testing: The measured flow speed is shown. The predicted skin friction and boundary layer thickness are computed using $1/7^{\text{th}}$ power law correlations.

Flow Speed (m/s)	Ma	Re _x (x10 ⁶)	C _f	δ (mm)	τ _w (Pa)
17.4	0.05	0.74	0.0039	15	0.56
34.4	0.10	1.5	0.0036	14	2.5
52.0	0.15	2.2	0.0034	13	5.3
61.7 (max)	0.18	2.6	0.0033	13	7.6

At each flow condition, a traversing pitot/static probe was used to measure the boundary layer profile. The results are presented in Figure 7. A best fit was produced to the boundary layer profiles as scaled by inner flow variables. As shown in the figure, for small y^+ , the data collapse onto the Law of the Wall. For $y^+ > 300$ the nondimensional velocity increases above the law of the wall as we enter the outer layer. Cole's Law of the Wake was used to fit the data, since the data is primarily in the outer layer [15],

$$u^+ \approx \frac{1}{\kappa} \ln(y^+) + B + \frac{2\Pi}{\kappa} f\left(\frac{y}{\delta}\right) \quad (10)$$

where u is the measured flow velocity, y is the physical distance from the wall, $u^+ = u/v^*$ is the nondimensional velocity, $y^+ = yv^*/\nu$ is the nondimensional distance from the wall, $\kappa = 0.41$ and $B = 5.0$ are the von Karman Law of the Wall constants, and the function $f()$ is an S-shaped function that is used to model the deviation of the velocity profile from the log law in the outer layer. The functional form used here was taken from [15]

$$f(\eta) = \sin^2\left(\frac{\pi}{2}\eta\right) \quad (11)$$

Cole's wake parameter was taken to be $\Pi = 0.5125$ since the streamwise pressure gradient is very small (measured via static pressure taps in the floor to be less than 0.12 Pa/mm at the highest flow rate) [15]. There are two free parameters remaining, the boundary layer thickness, δ , and the friction velocity, v^* . A two dimensional optimization was performed on these parameters to minimize the residual between the measured boundary layer profile and the Law of the Wake. The optimization was not very sensitive to δ so this parameter is less easily measured. However v^* had a smaller optimal region and was better measured. Since surface shear depends on v^* , surface shear appears to be reasonably well determined, although no error bounds have been derived. Once v^* is estimated, the surface shear stress is known,

$$\tau_w = \rho v^{*2} \quad (12)$$

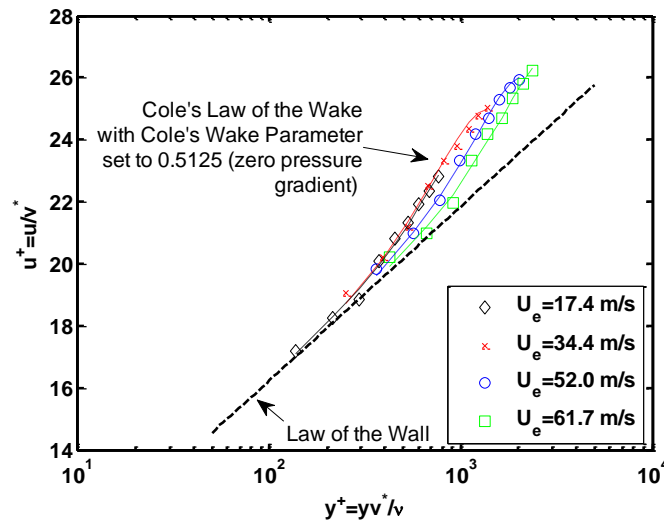


Figure 7: Boundary layer profiles measured at each flow condition using a pitot/static probe scaled by inner layer variables. Best fit to Cole's Law of the Wake.

Table 3. Flow conditions for tunnel testing: The measured flow speed is shown. The best fit friction velocity and velocity boundary layer thickness are shown based on the numerical fit to Cole’s Law of the Wake. Wall shear stress is computed from friction velocity.

Flow Speed (m/s)	v^* (m/s)	δ (mm)	τ_w (Pa)
17.4	0.75	25	0.7
34.4	1.37	13	2.3
52.0	1.99	14	4.8
61.7 (max)	2.32	18	6.5

The shear stresses computed from the boundary layer profiles (Table 3) are similar, but not identical, to those predicted by the $1/7^{\text{th}}$ power law correlation for the zero pressure gradient turbulent flat plate (Table 2). In order to estimate real time wall shear stress for a direct comparison to the MEMS sensor output, a quadratic fit was used between the freestream flow speed and the wall shear stress of Table 3. The fit is shown in Figure 8.

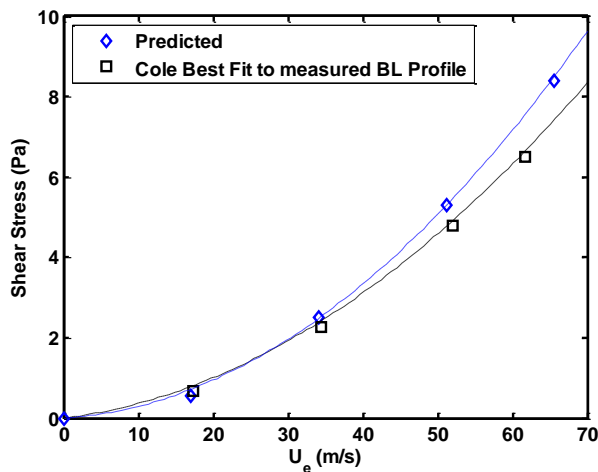


Figure 8: Shear stress plotted vs. velocity as predicted from flat plate $1/7^{\text{th}}$ power law correlation and as determined from the fit to the boundary layer profile.

The tunnel was run between these conditions, stepping up, then holding at the maximum speed, stepping down to minimum speed, back up to maximum speed, and so on for 4 cycles before stepping down through the four speeds back to zero. Three tests were run: one with the sensor aligned with the flow, one with the sensor aligned opposite the flow, and one with the sensor aligned in the cross-flow direction. The results are shown in Figure 9. The sensor accurately captures the changing shear stress in real time. When rotated opposite to the flow, the sign flips on the output, as expected. When oriented in the cross-flow direction, no change is observed in the sensor output. This is a strong indication that the sensor is measuring shear, and not temperature, humidity, or other scalar quantities. In addition, the measured streamwise pressure gradient in the duct is low, less than 0.12 Pa/mm, so it seems unlikely that the sensor is responding to pressure gradient rather than shear stress.

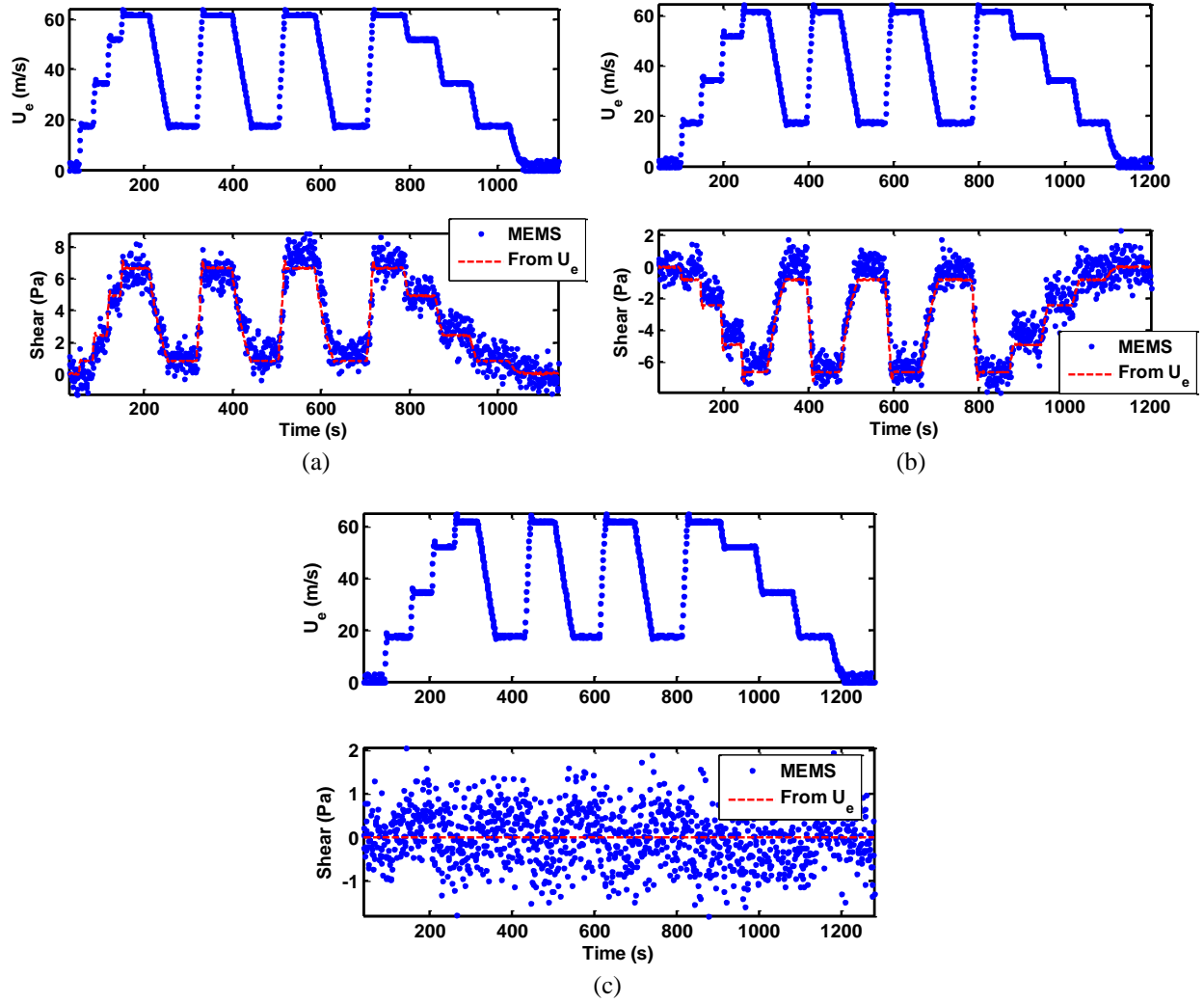


Figure 9: Flow test results. The top panels in each plot show the free stream velocity measured by the pitot/static probe. The bottom panels show a comparison between the measured shear stress from the MEMS sensor, and the shear stress computed from the velocity using the correlation from Figure 8. (a) MEMS sensor oriented with the flow. (b) MEMS sensor oriented opposite to the flow direction. (c) MEMS sensor oriented in the cross-flow direction.

The best fit between the MEMS output and the shear computed from velocity is achieved with a sensitivity of 90 aF/Pa. Laminar flow calibrations reported previously gave similar results [14, 16]. Referring back to equation (6) and the measured dimensions of the element in Table 1, and noting that the current chip has 128 active elements (half of the elements on the chip are being used), the approximate expected sensitivity can be computed based on the physical surface area of the shuttle,

$$S_2 \approx 128 \frac{N \varepsilon L^3}{E d w^3} A_m = 128 \frac{64 \left(8.85 \cdot 10^{-12} \frac{F}{m} \right) (99 \mu\text{m})^3}{205 \text{GPa} \cdot 2.9 \mu\text{m} \cdot (5.1 \mu\text{m})^3} 0.085 \text{mm}^2 = 76 \text{aF} / \text{Pa} \quad (13)$$

This approximate expected sensitivity is close to the best fit result from the tunnel tests. The difference between the sensitivity predicted from (13) may come from two sources: (i) experimental error in surface shear, dominated by

the accuracy of the boundary layer profile data and the model fit to the boundary layer profile used to extract the wall shear from flow velocity (ii) neglecting the effects of the surface bumps and sensor topology on the fluid interaction forces. Recent computational fluid dynamics work by our group on this geometry, reported elsewhere [17], suggests that the surface topology does play a measurable role in determining sensitivity, so equation (13) should be taken as a simplified approximate computation.

In the reported test, pressure gradient sensitivity was not a concern as pressure gradient was very low. However, other experimental work by our group indicates that pressure gradient sensitivity for a device such as this is on the order of $16 \text{ aF}/(\text{Pa}/\text{mm})$ [16]. If substantial pressure gradients were present in the test environment pressure gradient would need to be measured separately and corrected for.

A slow drift in the capacitance of the MEMS sensor was experienced. Between 0.2-0.5 aF/second were experienced in the three runs described here. This is equivalent to a drift of approximately 0.1-0.3 Pa/minute. The output shown in Figure 9 was detrended by subtracting out a linear fit between the data at zero flow condition at the beginning and end of the run. This effectively removes the majority of the drift.

The temperature in the tunnel during the run was between 20°C and 22°C as measured by a thermocouple in the flow. The temperature of the MEMS sensor electronics was more stable, varying between 21°C and 21.5°C , as measured by the internal temperature sensor in the AD774x. No correlation was seen between temperature and sensor output in tunnel testing. However, more recent results do show both temperature and humidity sensitivity for the device, issues that will be explored in future work.

The standard deviation of the capacitance about the mean for the time domain data gives the noise density of the measurement. In a no flow condition, mounted in the tunnel in an identical setup to that used for flow testing, the measured standard deviation of measured shear stress was 0.8 Pa with a 1 Hz sample rate. A plot of the power spectral density of the capacitance noise shows that it is white noise. Hence, the noise density of the measurement is related to the standard deviation by

$$P_x = \sqrt{\frac{2\sigma^2}{F_s}} \quad (14)$$

where P_x is the noise density in $\text{Pa}/\sqrt{\text{Hz}}$, σ is the standard deviation in Pa, and $F_s=1$ is the sample rate in samples/second. The noise density of the capacitance measurement is therefore $1.1 \text{ Pa}/\sqrt{\text{Hz}}$ at low frequencies (below 0.5 Hz). An identical calculation performed on the data for the cross-flow case shown in Figure 9 (c) results in $0.9 \text{ Pa}/\sqrt{\text{Hz}}$. Thus, the fluctuations in shear shown in Figure 9 (c) are electronic noise, not real fluctuating shear stress components.

The measured resolution of approximately $1 \text{ Pa}/\sqrt{\text{Hz}}$ is equivalent to $90 \text{ aF}/\sqrt{\text{Hz}}$, but the manufacturer reports a resolution of $1.5 \text{ aF}/\sqrt{\text{Hz}}$ for the AD7745 chip. More work needs to be done to determine sources of additional noise, such as EMI, power supply fluctuations, or ground noise. In addition, a dynamic model of the element needs to be produced so that thermal-mechanical noise can be computed to determine if this is a major contributing factor.

IV. Conclusions

A MEMS floating element shear sensor with direct digital readout has been demonstrated in turbulent flat plate wind tunnel testing. The sensor is able to measure surface shear stress in real time in tunnel flow conditions with a resolution of $1 \text{ Pa}/\sqrt{\text{Hz}}^{1/2}$, a data rate of 3 samples per second, and a linear range of greater than 6.5 Pa. Laminar flow testing not reported here demonstrates linearity to greater than 13 Pa. Nonlinearities have not been observed for the achievable shear stresses generated in testing thus far. Some drift is observed, although this is effectively removed using a calibration procedure.

Future work will include demonstration of operation in a variety of flow conditions, additional testing on temperature and humidity sensitivity, and system improvements to increase resolution, accuracy, and sampling rate.

Acknowledgments

This work was supported by a contract from Spirit Aerosystems, Wichita, KS. Tunnel testing was made possible by a sabbatical leave granted by Tufts University during which R. W. was hosted by NASA Ames Research Center, Fluid Mechanics Lab.

References

1. J.W. Naughton and M. Sheplak, "Modern developments in shear-stress measurement", Prog. Aerospace Sci. 38 (2002) pp 515-570.
2. H. Fernholz, G. Janke, M. Schober, P. Wagner and D. Warnack, "New developments and applications of skin-friction measuring techniques", Measurement Science and Technology. 7 (1996).
3. K. G. Winter, "An outline of the techniques available for the measurement of skin friction in turbulent boundary layers" Progress in aerospace sciences, vol. 18, pp. 1-57, (1979).
4. L. Tanner and L. Blows, "A study of the motion of oil films on surfaces in air flow, with application to the measurement of skin friction", Journal of Physics E: Scientific Instruments. 9 (1976).
5. B. Van Oudheusden, "Silicon thermal flow sensors", Sensors and Actuators A: Physical. 30 (1992) pp 5-26.
6. L. Lofdahl, V. Chernoray, S. Haasl, G. Stemme, M. Sen, "Characteristics of a hot-wire microsensor for time-dependent wall shear stress measurements", Experiments in Fluids. 35 (2003) pp 240-251.
7. E. Kälvesten, C. Vieider, L. Löfdahl, G. Stemme, "An integrated pressure—flow sensor for correlation measurements in turbulent gas flows", Sensors and Actuators A: Physical. 52 (1996) pp 51-58.
8. M. A. Schmidt, R. T. Howe, S. D. Senturia, J. H. Haritonidis, and C. Mit, "Design and calibration of a microfabricated floating-elementshear-stress sensor" IEEE Transactions on Electron Devices, vol. 35, (1988).
9. A. Padmanabhan, H. Goldberg, K. D. Breuer, and M. A. Schmidt, "A wafer-bonded floating-element shear stress microsensor withoptical position sensing by photodiodes" Journal of Microelectromechanical Systems, vol. 5, (1996).
10. T. Pan, D. Hyman, M. Mehregany, E. Reshotko, and S. Garverick, "Microfabricated shear stress sensors, part 1: design and fabrication" AIAA Journal, vol. 37, (1999).
11. Chandrasekharan, V., Sells, J., Meloy, J., Arnold, D.P., Sheplak, M., "A metal-on-silicon differential capacitive shear stress sensor", in Solid-State Sensors, Actuators and Microsystems Conference, TRANSDUCERS (2009).
12. Zhe J, Modi V, Farmer KR.. "A microfabricated wall shear-stress sensor with capacitive sensing." J. Microelectromech. Syst. 14 (2005) pp 167–75
13. L. Lofdahl, M. Gad-el-Hak, "MEMS-based pressure and shear stress sensors for turbulent flows", Measurement Science & Technology. 10 (1999) 665-686.
14. Zhao, Z., Shin, M., White, R. D., and Gallman, J. "A MEMS Floating Element with Bump Shear Stress Sensor Array on a Chip" in the Proceedings of the 51st AIAA Aerospace Sciences Meeting, Grapevine, TX, Jan. 7-10. (2013) AIAA 2013-0626
15. F.M. White, Viscous Fluid Flow 3rd Edition, McGraw-Hill Education (2006).
16. Zhao, Z., Shin, M., Gallman, J. M., and White, R. D. "A Microfabricated Shear Sensor Array on a Chip with Pressure Gradient Calibration", Sensors and Actuators A: Physical. vol. 205, (2014) pp 133-142.
17. Kastor, N., Zhao, Z., and White, R. D. "Modeling of a MEMS Floating Element Shear Sensor" in the Proceedings of the Materials Research Society, MRS Fall Meeting, Boston, MA December1-6, 2013.